Parametrization protocol and refinement strategies for accurate and transferable analytic bond-order potentials: Application to Re

Aparna P. A. Subramanyam*
Interdisciplinary Centre for Advanced Materials Simulation (ICAMS), Ruhr-Universität Bochum, 44801, Germany and Theoretical Division T-1, Los Alamos National Laboratory, Los Alamos, New Mexico 87545, USA

Jan Jenke,* Alvin N. Ladines, Ralf Drautz, and Thomas Hammerschmidt
Interdisciplinary Centre for Advanced Materials Simulation (ICAMS), Ruhr-Universität Bochum, 44801, Germany

(Received 5 July 2023; accepted 14 November 2023; published 17 January 2024)

Interatomic potentials provide a means to simulate extended length and time scales that are outside the reach of *ab initio* calculations. The development of an interatomic potential for a particular material requires the optimization of the parameters of the functional form of the potential. We present a parametrization protocol for analytic bond-order potentials (BOPs) that provides a physically transparent and computationally efficient description of the interatomic interaction. The parametrization protocol of the BOP follows the derivation of the BOP along the coarse-graining of the electronic structure from density-functional theory (DFT) to the tight-binding (TB) bond model to analytic BOPs. In particular, it starts from TB parameters that are obtained by downfolding DFT eigenstates of two-atomic molecules to an *sd*-valent minimal basis. This *sd*-valent Hamiltonian is combined with a pairwise repulsion to obtain an initial binding energy relation. The *s* electrons are then removed from the Hamiltonian and instead represented by an isotropic embedding term. In the final step, the parameters of the remaining *d*-*d* interaction, the pair repulsion, and the embedding term are optimized simultaneously. We demonstrate that the application of this parametrization protocol leads to a basic BOP for Re with good transferability. We discuss different strategies to refine the basic BOP towards global transferability or towards local accuracy. We demonstrate that homogeneous samplings of the structural phase space in a map of local atomic environments can be used to systematically increase the global transferability. We also demonstrate the influence of training data weighting on local accuracy refinements with a Pareto-front analysis, and we suggest further requirements to select a final BOP. The local accuracy and global transferability of the final BOP is also shown and compared to DFT.

DOI: 10.1103/PhysRevMaterials.8.013803

I. INTRODUCTION

Quantum-mechanical calculations on the basis of density-functional theory (DFT) allow computational materials scientists in principle to predict all properties of structural and functional materials. In practice, however, the computational cost of DFT calculations limits this approach typically to system sizes of only a few hundred atoms. This limitation puts many material phenomena out of reach for DFT calculations, e.g., plastic deformation, melting, and phase transitions. One of the central goals of computational materials science at the atomistic scale is therefore to complement DFT calculations with computationally more efficient approaches. The two main approaches are to represent the DFT potential energy surface by numerical interpolation of a large number of data points and by physics-inspired models of the interatomic interaction.

The physics-inspired models require orders of magnitude fewer parameters to be adjusted in their construction. This leads to a significantly lower demand on the training data but also to less flexibility with regard to optimization to a set of training data. The robustness with regard to the predictions, therefore, depends on the physical ground of the functional form, the training data, and the parametrization strategy. Their subtle interplay is the core of the challenge of developing reliable parametrizations of physics-inspired models of the interatomic interactions [1–7].

The different models are formulated either as an explicit function of atomic positions for specific types of interactions, e.g., metals [8,9] or semiconductors [10,11], or as more flexible coarse-grained electronic-structure methods like tight-binding (TB) [12–15] or bond-order potentials (BOPs) [16–19]. Many published models exhibit quantitative and often qualitative differences in their prediction for the same material; see, e.g., Refs. [20–22] for extensive comparisons and benchmarks. Such comparative assessments are often challenged by the different and not always fully transparent choices of training data and parametrization strategy.

In this work, we propose a parametrization protocol for a basic model and different strategies towards refined models for the case of coarse-grained electronic-structure methods. We focus on an analytic BOP [23] that is derived by a second-order expansion of the energy functional from DFT to TB to BOP [19] and that has been shown to provide a robust description of transition metals with bcc [24–32] and fcc/hcp [33–37] ground-state structures.

*These authors contributed equally to this work.

The parametrization is carried out along an analogous coarse-graining route from downfolding DFT eigenstates of dimers to a TB Hamiltonian [38], the addition of a simple pairwise repulsion term, the replacement of *s*-electrons in the Hamiltonian by a simple embedding function, and the approximate solution of the TB Hamiltonian with an analytic BOP. An approach is introduced to analyze the transferability to other crystal structures in a transparent and intuitive way with a recently established map of local atomic environments [39]. Different strategies are compared to refine the resulting basic model obtained with few training data towards global transferability by adding a homogeneous coverage of phase space in the map or towards local accuracy by adding specific training data motivated by potential applications.

For the purpose of demonstrating our parametrization protocol, we choose Re with hcp as the ground state as the example material in this work. Re is often added to Ni-based superalloys to improve their creep properties [40]. In fact, the aircraft industry accounts for almost 70% of the world's consumption of industrially produced Re [41]. It also plays a role as product of nuclear transmutation of W under neutron irradiation of plasma-facing materials for divertors in fusion reactors [42]. In both applications, Re promotes the formation of complex intermetallic phases, particularly topologically close-packed (TCP) phases [40,43–46], that deteriorate the mechanical properties. There are only two existing models for Re based on the embedded-atom method (EAM) [47,48].

In Ref. [47], the model is fitted mainly to the elastic constants, the equation of state data for the ground-state hcp structure, along with the cohesive energies and lattice parameters of bcc, fcc, and hcp crystal structures. The resulting model describes the elastic constants well, but the self-interstitials were poorly described as shown in Ref. [48]. In Ref. [48], the Re model is explicitly fitted to several defect, liquid, and other crystal structures. This model performs very well for point defects but poorly describes the elastic constants with differences to reference experimental values reaching as high as 270 GPa for some elastic constants. In this regard, we show that our model for Re balances all the properties of interest satisfactorily.

A brief summary of methodology and reference data is given in Sec. II. In Sec. III, we outline the parametrization along the same coarse-graining route by downfolding DFT eigenstates of dimers to a TB Hamiltonian, which is then simplified and solved approximately with an analytic BOP. In Sec. IV, the resulting basic BOP is refined with different strategies towards global transferability and local accuracy. The compromise between the two strategies is worked out by identifying the Pareto front for different weighting of training data and by determining the transferability across a broad range of local atomic environments. Using additional tests, a final BOP for Re is selected in Sec. V and compared to DFT reference data.

II. METHODOLOGY

A. Analytic bond-order potentials

The analytic bond-order potentials are derived by coarse-graining the description of the electronic structure from DFT to the tight-binding (TB) bond model [13] to the BOP [19,23]. For a nonmagnetic, charge-neutral system, the most basic form of the total binding energy (E_{bind}) in the TB bond model is written as

$$E_{\mathrm{bind}} = E_{\mathrm{bond}} + E_{\mathrm{rep}}, \tag{1}$$

where E_{bond} and E_{rep} are bonding and repulsive energy, respectively. Further terms due to magnetism and charge transfer [19,49] are not required for the application to Re in this work.

The bond energy E_{bond} is calculated by integrating the local density of states $n_{i\alpha}(E)$ of orbital α on atom i up to the Fermi level E_F as

$$E_{\mathrm{bond}} = 2\sum_{i\alpha}\int_{-\infty}^{E_F}(E - E_{i\alpha})n_{i\alpha}(E)dE \tag{2}$$

with the energy of the atomic on-site level $E_{i\alpha}$. In the BOP formalism, $n_{i\alpha}(E)$ is not obtained by diagonalization of the TB Hamiltonian $\hat{H}$ but by using the moments theorem [50] that relates the local electronic structure in terms of $n_{i\alpha}(E)$ to the local atomic structure. The Nth moment of $n_{i\alpha}(E)$ given by

$$\mu_{i\alpha}^{(N)} = \int E^N n_{i\alpha}(E)dE \tag{3}$$

can also be written as a product of pairwise Hamiltonian matrices along self-returning paths that start and end on atom i orbital α,

$$\begin{aligned}\mu_{i\alpha}^{(N)} &= \langle i\alpha|\hat{H}^N|i\alpha\rangle \\ &= \sum_{j\beta\cdots}\langle i\alpha|\hat{H}|j\beta\rangle\,\langle j\beta|\hat{H}|k\gamma\rangle\,\langle k\gamma|\hat{H}|\cdots\rangle\,\langle\cdots|\hat{H}|i\alpha\rangle \\ &= H_{i\alpha j\beta}H_{j\beta k\gamma}H_{k\gamma\ldots}H_{\ldots i\alpha},\end{aligned} \tag{4}$$

where $H_{i\alpha j\beta}$ is the orthogonal TB Hamiltonian that describes the interaction between atom i orbital α and atom j orbital β. Details of the computation of E_{bond} from $H_{i\alpha j\beta}$ are given elsewhere [49]. The construction of $H_{i\alpha j\beta}$ is a central part of the TB/BOP parametrization. For most BOP models, the values of $H_{i\alpha j\beta}$ are derived from DFT calculations and kept fixed in the parametrization [29,30,35]. The TB Hamiltonians for *sd*-valent systems are often simplified by replacing the *s* contribution in the Hamiltonian with an additional attractive embedding energy E_{emb} [26,28], as described in detail below.

The attractive bond energy of a TB/BOP model is balanced by repulsive contributions E_{rep} that represent the overlap repulsion of atomic orbitals and higher-order terms. The simplest form of E_{rep} is a repulsive pair potential. More sophisticated forms of E_{rep} such as a Yukawa-like term [51,52] account for environment-dependent many-body repulsion [29,35]. The interaction range of the TB/BOP model is limited by multiplying bond integrals and pair repulsion with a cosine-shape cutoff function [49] in the range of $[r_{\mathrm{cut}} - d_{\mathrm{cut}}, r_{\mathrm{cut}}]$. For Re in this work, we use $r_{\mathrm{cut}} = 6$ Å and $d_{\mathrm{cut}} = 0.5$ Å.

The further settings of the analytic BOP model developed in this work follow previous parametrizations for transition metals [30–32,36,37]. In particular, we use nine calculated moments, higher moments estimated up to 100,

and a square-root terminator with a Jackson kernel to ensure a strictly positive DOS. The calculations are performed self-consistently with numerically enforced charge-neutrality as described, e.g., in Ref. [19]. The calculations are carried out with BOPFOX software [49], which provides a linear scaling of the computational effort with the number of atoms.

B. Parametrization setup

The parametrization of an interatomic potential in general, or a TB/BOP model in particular, requires us to adjust the free parameters such that the chosen set of training data is reproduced with sufficient accuracy. The underlying numerical procedure uses a cost function that measures the discrepancy between the predictions of the potential and the reference data. A natural choice for the cost function is the root-mean-square (RMS) error

$$c(\boldsymbol{\theta}) = \sqrt{\frac{\sum_k^{N_{\text{ref}}} e_k^2}{N_{\text{ref}}}}, \tag{5}$$

where

$$e_k = w_k(E_{\text{pred},k}(\boldsymbol{\theta}) - E_{\text{ref},k}). \tag{6}$$

N_{ref} is the number of reference data points, $\boldsymbol{\theta}$ is a vector of model parameters, and $E_{\text{pred},k}(\boldsymbol{\theta})$ is the model prediction for structure k for given model parameters. $E_{\text{ref},k}$ is the corresponding reference, and w_k is a weight factor to balance the relative importance of structure k. We use a local minimization procedure, the Levenberg-Marquardt algorithm [53–55], to minimize the cost function $c(\boldsymbol{\theta})$. The minimization is implemented in the BOPCAT software [7] that drives BOP calculations with the BOPFOX software. The parametrization of the BOP model is carried out in two steps. In the first step, a basic BOP model is constructed with a small set of training data. In the second step, the basic BOP model is refined and validated against the full set of reference data.

C. Reference data

The reference data for the parametrization of the analytic BOP for Re in this work are total energies obtained from DFT calculations. These energies are computed using non-spin-polarized DFT calculations with VASP [56–58]. The projector augmented-wave (PAW) [59] method is used with the generalized gradient approximation [60]. A high accuracy of the calculations is obtained by a plane-wave cutoff energy of 400 eV and Monkhorst-Pack [61] k-point meshes with a linear density of 0.125 Å^{-1}.

The reference data cover ideal crystal structures including the basic structures hcp, dhcp, fcc, bcc as well as the topologically close-packed (TCP) phases A15, C14, C15, C36, σ, μ, and χ that are known to form as Re-compounds (see, e.g., Refs. [43,62]) or as Re-containing precipitates in Ni-based superalloys (see, e.g., Ref. [40]). The energy-volume curves for the different crystal structures are computed for 20 structures within ±20% of the equilibrium volume and fitted to fifth-order polynomials for obtaining the equilibrium volume, energy, and bulk modulus. For the hcp ground state, we additionally include the elastic constants (using 14 structures within strain rates of up to ±2% along each elastic deformation). The energy-volume curves for all the crystal structures along with the elastic constants for the ground-state hcp structure were obtained using pyiron [63]. To assess the transferability of the BOP model, we furthermore consider the defects shown in Fig. 1: (i) vacancies and the different self-interstitial atom (SIA) configurations, (ii) vacancy diffusion-paths within the basal plane and perpendicular to it computed with the nudged-elastic-band method [64,65], (iii) basal (0001) and prismatic (10$\bar{1}$0) surfaces, as well as (iv) the basal intrinsic stacking fault and the extrinsic stacking fault that are related to plastic deformation [66–68].

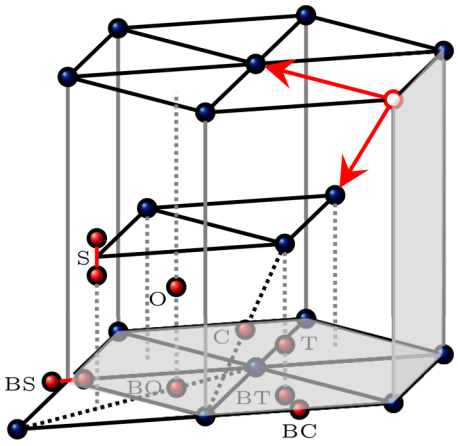

FIG. 1. Defects in hcp crystal structures: Self-interstitial atoms in crowdion (C), octahedral (O), split dumbbell (S), tetrahedral (T), basal crowdion (BC), basal octahedral (BO), basal split dumbbell (BS), and basal tetrahedral (BT) configuration (red atoms); vacancy (red circle) and vacancy diffusion paths (red arrows); and basal (0001) and prismatic (10$\bar{1}$0) surfaces (shaded in gray). Adapted from Ref. [48].

III. PARAMETRIZATION OF THE INITIAL BOP MODEL

A. Initial guess

The parametrization of the BOP model, as of many other interatomic potentials, corresponds to a nonlinear optimization problem. One can therefore expect multiple local minima of the cost function [Eq. (5)] in the space of model parameters. Searching the global minimum usually involves prohibitive computational cost, and therefore local minimization algorithms are common practice. This leads, however, to a potential dependence of the optimized model parameters on the initial guess of their values that is needed to start the local minimization. A physically sound initial guess is therefore required as it more likely leads to a physically meaningful local minimum.

For BOP models, we can construct a physically motivated initial guess for the Hamiltonian $H_{i\alpha j\beta}$ by utilizing downfolded DFT eigenstates of Re-Re dimers to a minimal basis with sd orbitals [38]. The $ss\sigma$, $sd\sigma$, $dd\sigma$, $dd\pi$, and $dd\delta$ matrix elements of the orthogonal sd-valent Hamiltonian are computed for different bond lengths and parametrized as

$$H(R) = \sum_i c_i \exp(-\lambda_i R^{n_i}), \tag{7}$$

with R the distance between the two atoms of the Re-Re dimer. The on-site matrix elements are taken from the values of the free atom computed from the asymptotic values of the parametrizations for large dimer bond-lengths R. The down-folded $H_{i\alpha j\beta}$ show good ad hoc transferability to different crystal structures [26,28,32,37,38] and will be further optimized during the parametrization process in this work. This work focuses on Re, but the approach is general and the down-folded $H_{i\alpha j\beta}$ are available in a database for all homovalent and heterovalent dimers across the Periodic Table [38].

Further parameters to be set are the number of s and d valence electrons of the BOP model. We estimate the number of electrons with s and d character by projecting the DOS obtained from DFT calculations for hcp-Re on s and d orbitals, respectively. The resulting values are 0.77 s-electrons and 5.30 d-electrons. During the optimization procedure we adjust the number of d-electrons to 5.70. The total number of valence electrons in the BOP model, $N_e = 6.47$, is in close agreement with the $5d^5 6s^2$ electronic configuration of the Re pseudopotential of the DFT calculations.

B. Parametrization protocol

The BOP methodology is a coarse-grained description of the electronic structure and thereby provides a certain degree of intrinsic robustness and transferability. The goal of the parametrization protocol in this section is to construct a basic BOP parametrization with minimal model complexity and minimal training data. Due to the underlying physics, the basic BOP reaches good robustness and transferability already at this low level of parametrization. From this level, the basic BOP can be further refined by increasing model complexity and training data as shown in the next section or serve as a common starting point for the development of compound models. The parametrization protocol is summarized in Fig. 2 and explained step-by-step in the following. The only training data used for the basic BOP are the energy-volume data of hcp, fcc, and bcc crystal structures. The parametrization progress in describing this minimal set of training data during execution of the parametrization protocol is compiled in Fig. 3.

1. Step 1: Initial sd-valent Hamiltonian

In the first step of the parametrization protocol, the BOP model includes only the bond energy [Eq. (2)] computed with the initial sd-valent Hamiltonian $H_{IJ}^{\mathrm{ini},sd}$ from the down-folded DFT eigenstates. In the absence of a repulsive counterpart, the energy-volume curves exhibit no minimum and cannot be compared directly to DFT, as shown in Fig. 3(a). The differences in the BOP and the DFT energy-volume curves are comparable, however, by using the structural energy-difference theorem [69,70]. For the development of BOP models, this is particularly useful for verification of the number of valence electrons (see, e.g., Refs. [30,71]) in an early stage of the parametrization.

2. Step 2: Addition of a repulsive pair potential

In the second step, the BOP model is extended to include a repulsive part that counteracts the purely attractive bond

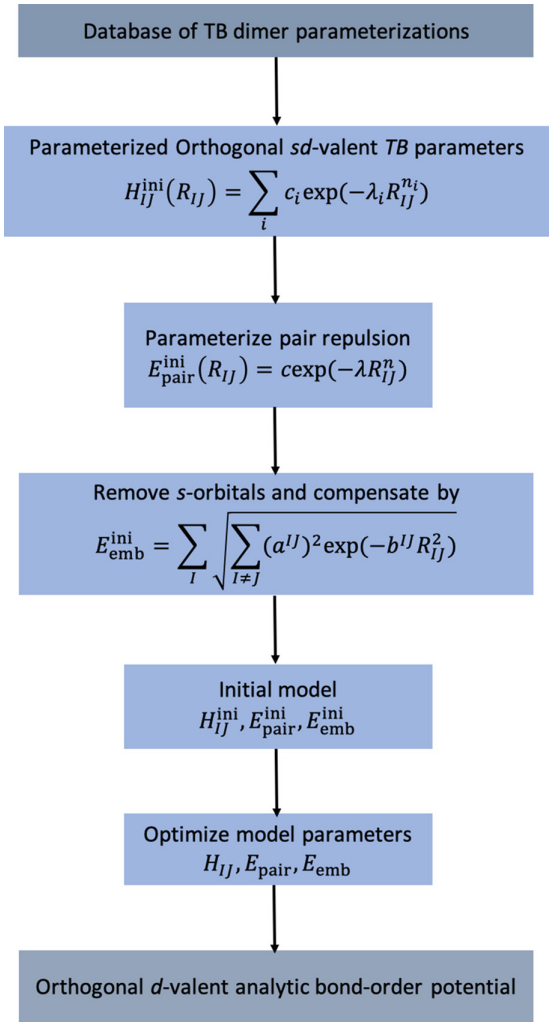

FIG. 2. Parametrization protocol for constructing a basic BOP model for sd-valent systems.

energy of the sd Hamiltonian. With the explicit treatment of s-electrons in the Hamiltonian, we add only a pairwise term with flexible functional form similar to the Hamiltonian matrix elements [Eq. (7)] as a repulsive part

$$E_{\mathrm{pair}} = \sum_{I\neq J} c_{\mathrm{rep}} \exp\left(-\lambda_{\mathrm{rep}} R_{IJ}^{n_{\mathrm{rep}}}\right) \tag{8}$$

with the distance R_{ij} between atoms i and j. The parameters c_{rep}, λ_{rep}, and n_{rep} are adjusted by optimizing the cost function [Eq. (5)] for the hcp, fcc, and bcc crystal structures while $H_{IJ}^{\mathrm{ini},sd}$ is kept fixed. In this step and in step 3, we performed optimizations with different random initialization in order to verify that the optimization converges to the same minimum.

At this level, the BOP model is able to capture the overall character of the interatomic interaction. This manifests in the correct qualitative energetic ordering of the three crystal structures [see Fig. 3(b)] and the correct range of formation energies. The quantitative performance will be improved in step 4.

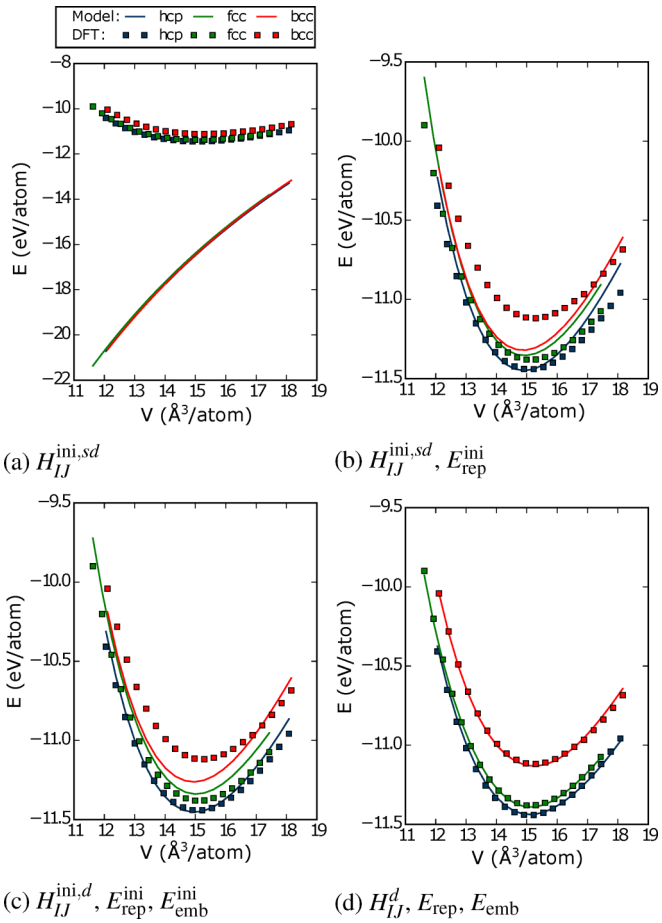

FIG. 3. Parametrization progress of the basic BOP model with minimal complexity and minimal reference data. Starting from (a) the initial *sd* Hamiltonian $H_{IJ}^{\mathrm{ini},sd}$, (b) the pairwise repulsion $E_{\mathrm{rep}}^{\mathrm{ini}}$ is added and optimized to the DFT reference data, (c) the energy contribution of *s*-electrons is replaced by an embedding term $E_{\mathrm{emb}}^{\mathrm{ini}}$, and (d) all parameters are optimized to the basic BOP model with H_{IJ}^{d}, E_{rep}, and E_{emb}.

3. Step 3: Removal of s-orbitals in Hamiltonian

Step 3 of the parametrization protocol is devoted to a simplification of the *sd* Hamiltonian by removing the *s*-electrons that do not play a significant role for a transition metal like Re. Other chemical elements may require an explicit treatment of the *s*-electrons, particularly if the interatomic interaction is governed by *sd*-hybridization. This step is computationally attractive not only with regard to the size of the Hamiltonian, but it also allows a lowering of the cutoff if only the less extended *d* orbitals participate in the interaction that directly translates to an increase in computational efficiency. The *s*-electrons are removed from the BOP model by taking out the corresponding *ss* and *sd* matrix elements from the Hamiltonian and by adjusting the number of valence electrons to $N_{\mathrm{e}} = 5.70$. The cutoff of the BOP model is reduced from $r_{\mathrm{cut}} = 6.0$–4.45 Å. The missing contributions to the bond energy are compensated by adding an additional attractive term. Here, we use an embedding term

$$E_{\mathrm{emb},s} = -\sum_{I} \sqrt{\sum_{J\neq I} (a_{\mathrm{emb}})^2 \exp\left(-b_{\mathrm{emb}} R_{IJ}^2\right)} \qquad (9)$$

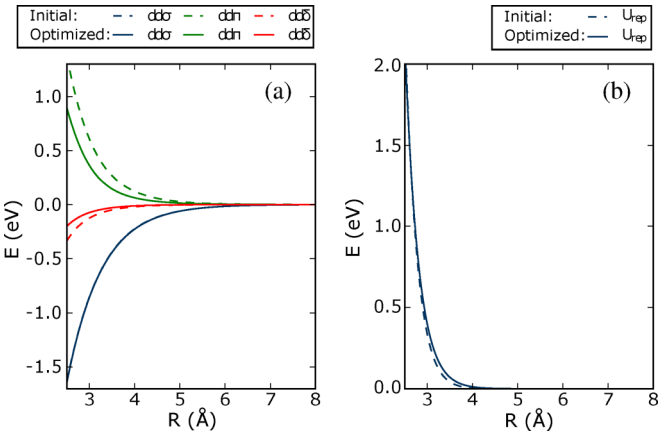

FIG. 4. Comparison of (a) matrix elements H_{IJ} and (b) pair repulsion E_{rep} of initial BOP (dashed) and basic BOP (full) obtained by the parametrization protocol for Re hcp, fcc, and bcc reference data.

motivated by the attractive part of embedded-atom models. The parameters of the embedding term a_{emb} and b_{emb} are optimized to the hcp, fcc, and bcc crystal structures while all other parameters are kept fixed.

The comparison of Fig. 3(c) with Fig. 3(b) shows clearly that the contribution of *s*-electrons in Re-Re interactions can be replaced by a simple embedding term without a sizable loss of model quality. This point of the parametrization protocol concludes with the initial BOP model with a first parametrization of the complete functional form.

4. Step 4: From initial BOP to basic BOP

In this last step, the parameters of all terms, i.e., H_{IJ}^{ini}, $E_{\mathrm{rep}}^{\mathrm{ini}}$, and $E_{\mathrm{emb}}^{\mathrm{ini}}$, are optimized simultaneously to the hcp, fcc, and bcc training data. The resulting orthogonal *d*-valent analytic BOP is referred to as the basic BOP. The optimization of all BOP parameters leads to very good agreement with the DFT data, as shown in Fig. 3(d). The quality of the initial BOP model becomes apparent by realizing that the parameters change only slightly in this last optimization step, as shown for the matrix elements and the repulsive energy in Fig. 4. The effective decrease of the range of the matrix elements may be attributed to screening effects that play a role in the bulk reference data but were absent in the downfolding for dimers.

C. Transferability analysis of the basic BOP

The basic BOP obtained by the parametrization protocol is optimized for a minimum set of reference data, and it calls for an assessment of the transferability to other crystal structures and other properties. Here, we use 300 random structures that cover the full space of local atomic environments of one-atom unit cells in a homogeneous sampling. These structures were identified earlier in the construction of a map of local atomic environments that is spanned by descriptors based on BOP moments [39].

The comparison of the equilibrium energy and equilibrium volume of the random structures predicted by the basic BOP model and the DFT reference data is compiled in Figs. 5(a)

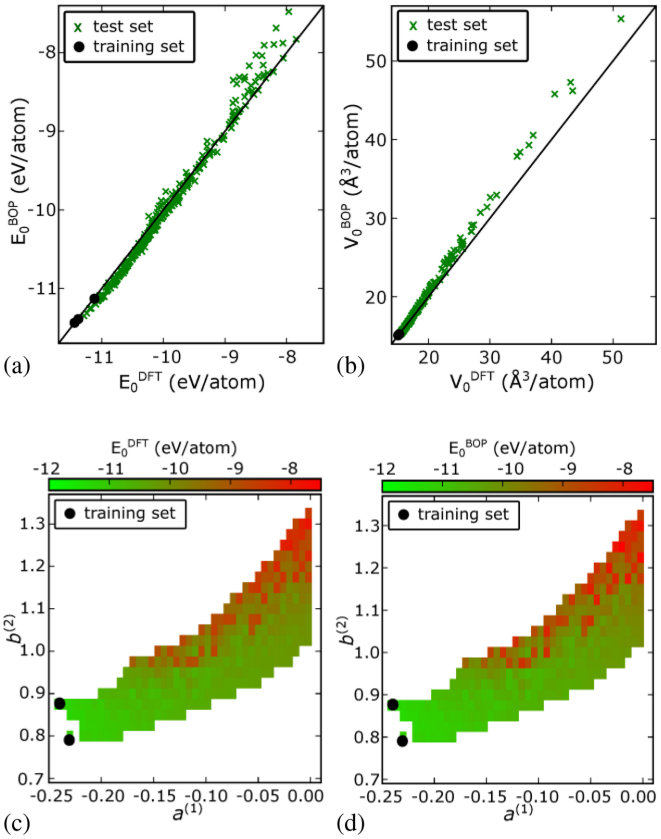

FIG. 5. Transferability of basic BOP to (a) equilibrium energy and (b) equilibrium volume of 300 random structures with one-atom unit cells as compared to DFT reference data. Variation of equilibrium energy across the complete range of local atomic environments in one-atom unit cells computed with (c) DFT and (d) basic BOP. The black dots indicate the training data of the basic BOP, i.e., hcp, fcc, and bcc crystal structures.

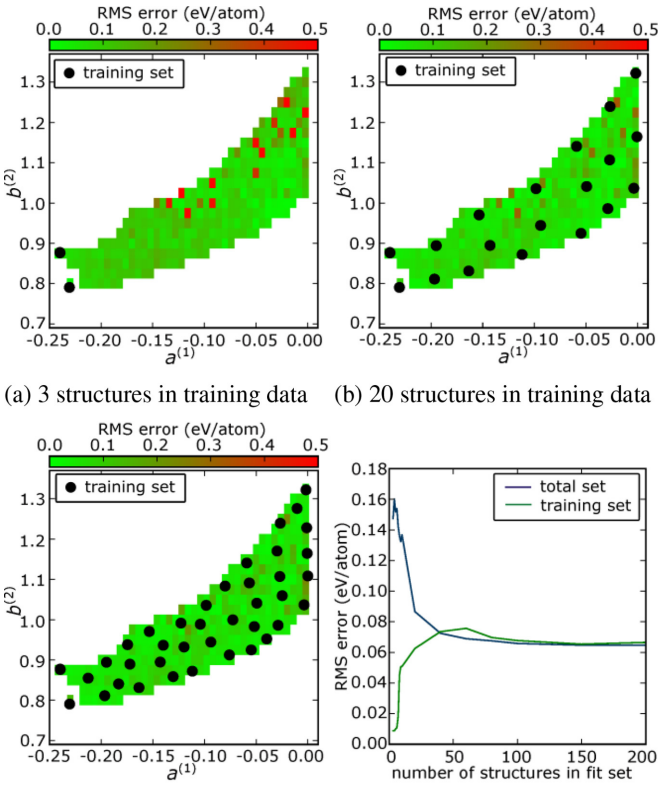

FIG. 6. Refinement of the basic BOP model towards global transferability. The RMS error (a) after optimization to hcp, fcc, and bcc improves systematically by homogeneous samplings of the space of local atomic environments using (b) 20 and (c) 40 random structures, and it shows saturation of the (d) learning curve at an RMSE of about 65 meV/atom.

and 5(b). The agreement across the entire range of structures can be considered excellent given that only the energy-volume curves of hcp, fcc, and bcc were used in the parametrization.

The assessments in Figs. 5(a) and 5(b) provide a relation between the basic BOP and the DFT reference data across the range of energies or volumes that is, however, agnostic of the corresponding atomic environments. Therefore, we additionally present the equilibrium energies obtained by DFT and the basic BOP as a color code in the structure similarity map in Figs. 5(c) and 5(d), respectively. The coordinates in the map correspond to descriptors based on the moments of the DOS [Eq. (4)] from the BOP that discriminate different crystal structures [72,73] and local atomic environments [39]. The direct relation between the distance of two points in the map that correspond to different crystal structures and the difference in the formation energy of these crystal structures has also been used successfully in machine-learning applications [74]. This analysis shows clearly that the basic BOP captures the equilibrium energy very well across the complete space of local atomic environments of one-atom unit cells. It is transferable in the region of close-packed crystal structures where it was parametrized but also in regions of open structures with high energies (e.g., simple cubic, 2D square lattice, and linear chain at $a^{(1)} = 0$; see Ref. [39] for more details). This analysis underlines the intrinsic transferability of even simple BOP models from minimal sets of training data. In the next section, we will discuss different strategies to refine this basic BOP to a final BOP for Re.

IV. REFINEMENT OF THE BASIC BOP

A. Strategy 1: Towards global transferability

In the present parametrization, we deliberately kept the complexity of the BOP model to a minimum. This allows us to perform a transparent analysis of the balance between global transferability and local accuracy that is an inherent compromise in many developments of interatomic potentials. With strategy 1, we demonstrate a route to a refinement of the basic BOP towards global transferability. To this end, we use the map of local atomic environments and analyze the RMS error in the equilibrium energy that we obtain having used only hcp, fcc, and bcc structures in the training data. The distribution of the RMSE shows that the basic BOP has less transferability for structures with large distance to the training data; see Fig. 6(a). In other words, the map quantifies and confirms graphically the expectation that larger errors in

energy are to be expected for further extrapolations from the training data used in the parametrization.

An apparent strategy to improve the global transferability is to extend the set of training data. The map of local atomic environments offers access to systematically carry out homogeneous and extensive samplings of the full range of local atomic environments. The basic BOP is refined by optimizing all parameters to extended sets of training data. In particular, we add the energy-volume curves of random structures that are selected to achieve homogeneous samplings of the atomic environments with increasing density. In Figs. 6(b) and 6(c), we see that the RMS error computed for all 300 structures is systematically reduced by successively extending the training data to 20 and 40 random structures. Repeating the refinements of the BOP for homogeneous samplings with up to 200 random structures leads to the learning curves shown in Fig. 6(d). We find that 40 random structures are already a good representation of the range of atomic environments of one-atom unit cells. The unusual behavior of a crossing of the two curves and a higher RMS error in the training data than in the total set of structures is an artefact of the special choice of the reference data. The learning curve converges to an RMS error of about 65 meV/atom, which corresponds to 1.8% of the energy range of the considered structures. These results demonstrate the iterative optimization of transferability to one-atom unit cells by systematic samplings of local atomic environments. Despite its benefits, this approach requires further work towards sufficiently complete sets of complex unit cells to cover the atomic environments relevant for other crystal structures (e.g., TCP phases), defects (e.g., vacancies), and property calculations (e.g., displacements for elastic constants).

B. Strategy 2: Towards local accuracy

With the second strategy, we demonstrate a refinement of the basic BOP towards the description of specific properties without actively enforcing global transferability as in the first strategy. Here, we choose the target properties as TCP phases and elastic properties motivated by typical applications of Re. The training data consist of hcp, fcc, bcc, A15, C15, and σ phases that ensure a certain variety of local atomic environments in terms of the 12-, 14-, 15-, and 16-fold coordination polyhedra of the nearest-neighbor shells in these structures. They also contain the energies of elastic deformations of the ground-state hcp structure. The remaining reference data (cf. Sec. II C) are used for testing the model.

An integral part of this optimization strategy is an appropriate balancing of the weights of target properties in the cost function [Eq. (5)]. For the energy-volume data of different crystal structures, we allow higher errors for structures that are energetically less favorable than the hcp ground state using

$$w_{\mathrm{struc}} = \exp\left(\frac{E^{(0)}_{\mathrm{hcp}} - E^{(0)}_{\mathrm{struc}}}{\Delta E}\right) \tag{10}$$

with the respective equilibrium energies per atom $E^{(0)}_{\mathrm{struc}}$. The denominator of $\Delta E = 0.1$ eV is chosen empirically and corresponds to a temperature of about 1200 K. For the elastic

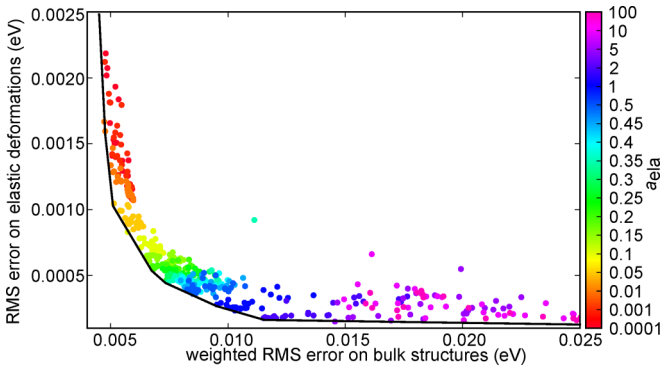

FIG. 7. RMS errors of bulk structures and of elastic properties of different BOP models (points) optimized with different weights a_{ela} of Eq. (11) (different colors), each starting from a set of different initial guesses (points of same color). The Pareto front (black line) indicates the balance of capturing these different properties.

properties, we introduce weights of

$$w_{\mathrm{ela}} = a_{\mathrm{ela}} \frac{\Delta E^{\mathrm{struc}}}{\Delta E^{\mathrm{ela}}} \tag{11}$$

to adjust the order of magnitude of the largest energy difference of the energy-volume curves $\Delta E^{\mathrm{struc}}$ (≈ 1 eV/atom) and the largest energy difference of the elastic deformations ΔE^{ela} ($\approx$50 meV/atom). Without this adjustment, the relative accuracy of the energy-volume curves will be higher than the elastic deformations due to their different range of energy.

For our assessment of the balance between global transferability and local accuracy, we use different values of a_{ela} in Eq. (11) that range from 0 (elastic deformations disregarded) to 100 (elastic deformations dominate optimization). For each value, we perform a set of optimizations to the 190 data points of the training data that start from 30 different initial guesses. The latter are generated by randomly changing the 23 parameters of the basic BOP model within a Gaussian distribution with a width of 5% of the initial parameter value. With the sets of randomized initial guesses, we enable the downhill optimization algorithm to detect more than only one local minimum in the high-dimensional parameter space.

Each of these optimizations leads to a BOP model that we assess with respect to the RMS errors of bulk structures and elastic properties comprising the training data as shown in Fig. 7. Overall, we observe the expected existence of a Pareto front. This marks the limit of optimizing one set of properties without compromising the other set, here bulk structures versus elastic deformations or vice versa. The close proximity of nearly all BOP models to the Pareto front demonstrates the overall robustness of the minimization procedure. The remaining scatter at the Pareto front confirms the existence of multiple local minima in the high-dimensional parameter space. The excellent capturing of bulk structures or elastic deformations for low or high values of a_{ela}, respectively, shows the effect of our training data weighting with Eq. (11). The minimum RMSE for bulk structures is less than 5 meV/atom, and for elastic deformations it is less than 0.1 meV/atom. The comparably high quality for bulk structures and elastic deformations across the whole Pareto front is an indicator of the intrinsic transferability of the BOP models. This analysis

shows that the refinement of the basic BOP model can be systematically targeted to a specific balance of the local accuracy for specific properties. The selection of one final BOP model from this set of candidate BOP models by additional criteria is discussed in the following.

V. SELECTION OF THE FINAL BOP

A. Selection criteria

For the selection of one model from the different optimizations in Fig. 7, we specify further criteria that are formulated as tests motivated by the material system Re. The numerical values of the quantitative tests are chosen empirically so as to minimize the number of models that pass all tests. We emphasize that different material systems and different applications will need qualitatively and quantitatively different tests. For Re in this work, the following tests are performed:

Test 1: Error in bulk structures below 0.05 eV or error in energy difference to hcp below 40%.

Test 2: Error in elastic constants below 90 GPa.

Test 3: hcp and dhcp structures correctly ordered.

Test 4: Error in c/a ratio of hcp below 0.01.

Test 5: Error in vacancy formation-energy below 0.8 eV.

Test 6: Error in vacancy diffusion-barrier within and in between basal planes below 0.5 eV.

Test 7: ISF formation energy larger than 20 $\mathrm{mJ/m^2}$.

Test 8: Error in SIA formation energies below 2.2 eV.

The performance of all BOP models of Fig. 7 on the individual tests is compiled in Fig. 8. Test 1 on the bulk structures is passed for models near the Pareto front with RMS error on bulk structures of less than about 10 meV/atom. Test 2 on elastic constants is passed by the majority of models across a broad range of RMSE values. Test 3 of the dhcp/hcp energy difference is passed by fewer models than test 2 on bulk structures as it requires resolving the hcp/dhcp energy difference of only 1.76 meV/atom in DFT. Test 4 on the c/a ratio is passed if the elastic deformations around the equilibrium are captured with sufficient accuracy. Test 5 on vacancy formation is passed for several models over a broad range of weights. Test 6 is passed by fewer models than test 5 as it additionally samples the different local atomic environments at the transition states of the diffusion paths. Tests 7 and 8 on defect formation show that the ISF can be captured by most models, while the SIA requires in most cases a high weight on bulk structures. Only two models near RMSE (bulk) = 0.005 eV and RMSE (elastic) = 0.001 eV pass all tests. The model with smaller RMSE (bulk) is selected as the final BOP for Re and assessed in the following. The optimized parameters of the final BOP model are given in Table I.

B. Assessment of the final BOP

To assess the local accuracy and the global transferability of the selected final BOP, an analysis is performed for the elastic constants and phonon spectrum of the hcp-Re ground state for point defects, stacking faults, and surfaces, as well as for the structural stability of TCP phases and random structures, and the BOP predictions are compared to DFT. The lattice parameters of the hcp ground state are very well captured by all potentials as shown in Table II. The elastic constants

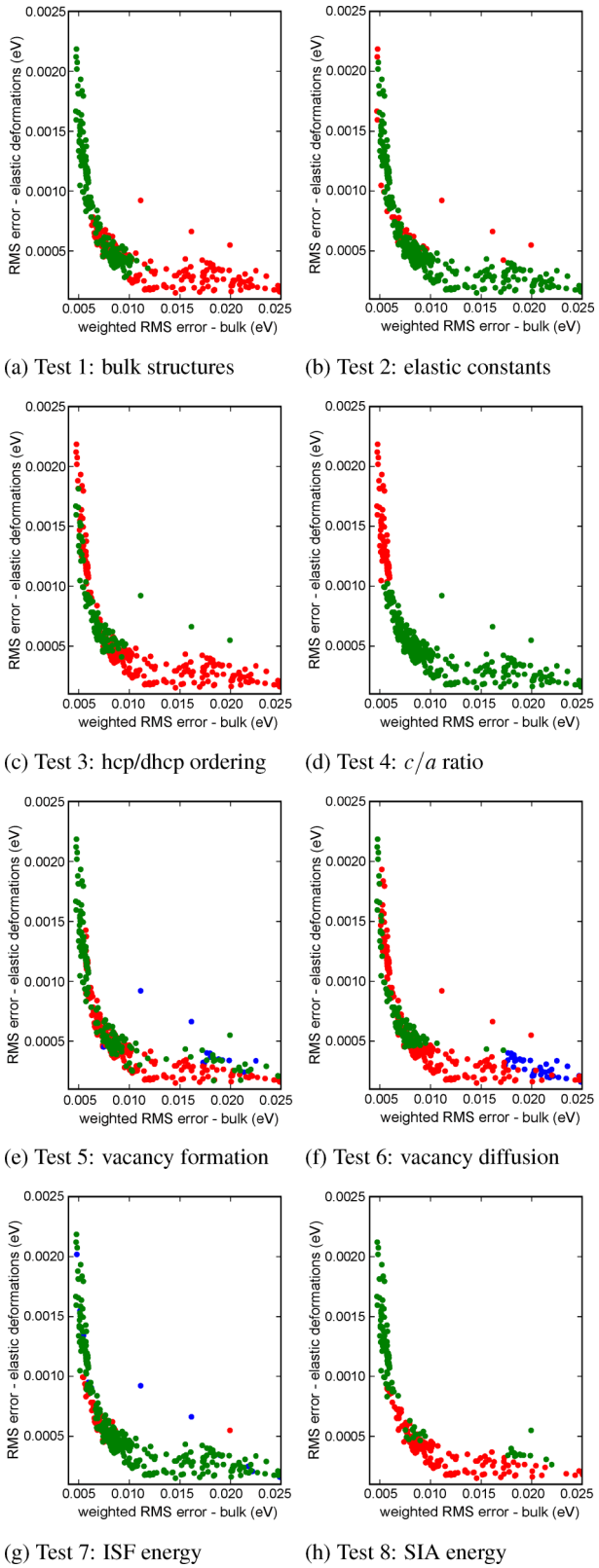

(a) Test 1: bulk structures (b) Test 2: elastic constants

(c) Test 3: hcp/dhcp ordering (d) Test 4: c/a ratio

(e) Test 5: vacancy formation (f) Test 6: vacancy diffusion

(g) Test 7: ISF energy (h) Test 8: SIA energy

FIG. 8. Performance of BOP models from Fig. 7 on test 1–8 with green/red signaling passed/failed tests. The points marked in blue correspond to the calculations that exceeded a maximal run time with respect to atomic relaxation.

predicted by BOP are overall in good agreement with DFT with the largest deviations for C_{12} and C_{33}.

TABLE I. Parameters of final BOP for Re used in the assessment in Sec. V B. The corresponding BOP functional form is given in Secs. II and III.

$H(R)$	c_0	λ_0	n_0	c_1	λ_1	n_1
$dd\sigma$	−25.6844	1.2112	0.9128	−0.0545	0.0022	5.8615
$dd\pi$	45.9185	1.5209	1.0781	1.3012	0.1368	2.8633
$dd\delta$	−11.8617	1.5604	0.9132	−9.7241	1.2671	1.7076
E_{pair}	c_{rep}	λ_{rep}	n_{rep}			
	65538.09	4.7264	0.8626			
E_{emb}	a_{emb}	b_{emb}				
	2.4338	0.1382				

As one of the indicators of the performance in finite-temperature simulations, we compute the phonon spectrum of Re-hcp, see Fig. 9, that was not included in the optimization procedure. The phonon density-of-states predicted by the final BOP is in good agreement with similar width but a small shift to higher frequencies. The phonon branches are overall in good qualitative agreement aside from the shift to higher frequencies.

The formation energies of points defects, stacking faults, and surfaces compiled in Table III sample the transferability to local atomic environments that were not included in the training data for optimizing the potential. The BOP correctly predicts the vacancy as the lowest-energy point defect. The energy barrier for vacancy diffusion in the basal plane is spot on, while the perpendicular path is less favorable in the BOP. The energetic ordering of SIA configurations is reproduced by the BOP except for the highest-energy basal tetrahedral. The absolute values of the formation energies are consistently overestimated by the BOP, which we expect to be improved by adding more training data with short interatomic distances. The formation energies of the stacking faults are in the correct order of magnitude and slightly underestimated by the BOP. The formation energies of the surfaces are accurate to ∼10% of the DFT values, showing that the BOP model can be applied to calculations of surfaces, where the local environment is different from the bulk.

TABLE II. Comparison of lattice parameters and elastic constants of the hcp ground state between DFT and BOP.

	DFT	BOP
a (Å)	2.782	2.786
c/a	1.617	1.608
C_{11} (GPa)	625	627
C_{12} (GPa)	232	303
C_{13} (GPa)	213	240
C_{33} (GPa)	677	592
C_{44} (GPa)	170	142
C_{66} (GPa)	196	162
$C_{12}-C_{66}$ (GPa)	36	141
$C_{13}-C_{44}$ (GPa)	43	98
B (GPa)	364	361

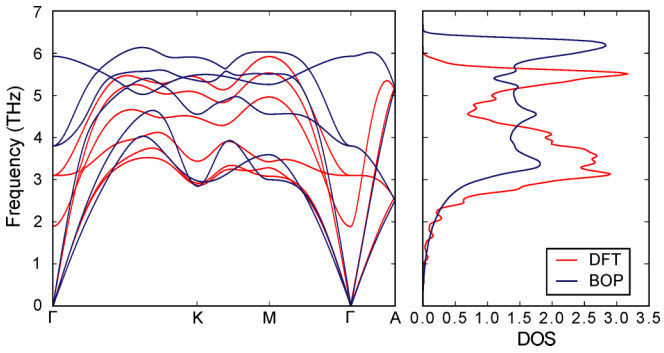

FIG. 9. Phonon spectrum and phonon density of states obtained by DFT and BOP.

The transferability to other bulk structures is quantified by comparisons for structures that are not in the reference data, particularly dhcp, TCP phases (C14, C36, μ, χ), and the random structures with one-atom unit cells (Fig. 5). The energy-volume curves of the structures in the reference data are reproduced very well [Fig. 10(a)] with bcc as the ground state and the correct ordering of all other structures. The larger deviations for the higher-energy structures A15 and C15 are a consequence of the energy-based weighting of reference structures with Eq. (10). The transferability of the BOP becomes apparent in the energy-volume curves of the structures that were not included in the reference data in Fig. 10(b). The dhcp structure is reproduced with high accuracy and all other structures with good accuracy and correct energetic ordering. The good transferability from the fitted TCP phases (A15, C15) to the tested TCP phases (C14, C36, μ, χ) can partly be attributed to the similarity of the local coordination polyhedra in this class of crystal structures.

The transferability of the BOP across the entire phase space of one-atom unit cells introduced in Sec. IV A is shown in Fig. 11. The transferability to close-packed structures is very good while the RMS error is considerably larger for open structures that are energetically less favorable for Re.

TABLE III. Comparison of planar and point defects for the ground-state hcp structure between DFT and BOP.

	DFT	BOP
Point defects (eV)		
Vacancy	3.22	3.91
Vacancy diffusion (basal plane)	2.02	2.02
Vacancy diffusion (perpendicular)	1.71	2.17
Tetrahedral SIA	6.76	8.93
Split dumbbell SIA	6.78	8.96
Octahedral SIA	8.16	9.46
Basal split dumbbell SIA	9.41	10.97
Basal tetrahedral SIA (BT)	10.17	10.44
Stacking faults (mJ/m^2)		
Intrinsic	55	21
Extrinsic	349	278
Surfaces (mJ/m^2)		
(0001)	2682	3005
$(10\bar{1}0)$	3904	4282

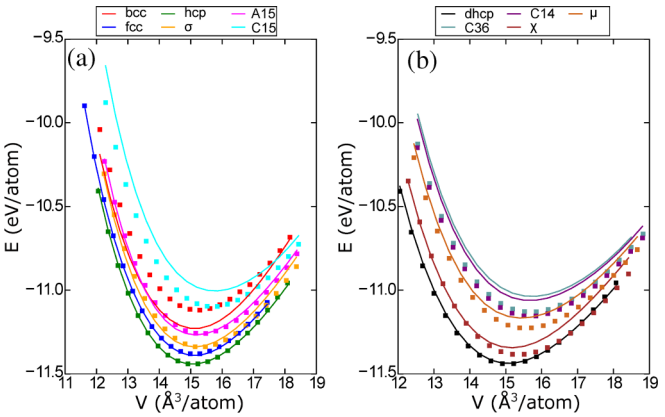

FIG. 10. Energy-volume curves of structures (a) in the training data set and (b) in the test set. DFT reference data are shown as symbols.

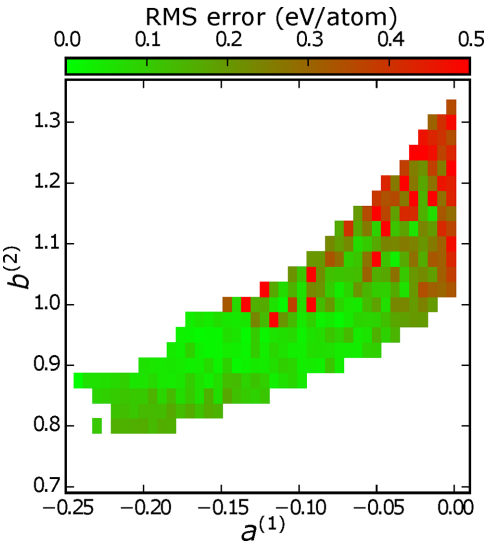

FIG. 11. Transferability of final model to random structures.

Comparing the RMS error of the final BOP to the RMS error of the basic BOP [Fig. 6(a)], we find a similar range of RMS error but a different distribution across the phase space of one-atom unit cells. The intrinsic transferability of the basic BOP that could be further improved with the first refinement strategy is apparently compromised in the second refinement strategy. The reason is the bias of the second strategy to the local atomic environments of elastic deformations and TCP phases. These are located at the lowest values of the phase space of one-atom unit cells (e.g., hcp at $a^{(1)} = -0.24$) or outside at even lower values of $a^{(1)} < -0.25$ as shown in Ref. [39]. The emphasis on high-precision for structures in this region leads to the larger RMS for the more open structures. The analysis with the RMSE in the map of local atomic environments highlights this difference between the two refinement strategies and provides transparent access to the balance of target properties.

VI. CONCLUSIONS

A parametrization protocol for analytic bond-order potentials is presented that is closely related to the underlying coarse-grained description of the electronic structure. Starting with an initial *sd*-valent Hamiltonian obtained by DFT calculations, a pairwise repulsion is added to establish an initial binding-energy relation. The Hamiltonian is simplified by replacing the contribution of the *s* electrons by an isotropic embedding term. A basic BOP is then obtained by all parameters to energy-volume data of hcp, fcc, and bcc. The good transferability of this basic BOP is demonstrated by a complete sampling of the phase space of one-atom unit cells using a map of local atomic environments.

Different strategies of refining the basic BOP are presented and compared. It is demonstrated that the global transferability across the phase space of one-atom unit cells can be systematically improved by simple homogeneous samplings with increasing density. An alternative strategy is presented of including elastic constants and further crystal structures in the optimization and shown to improve the local accuracy. The combination of the Pareto front for different weightings of the reference data with additional tests illustrates the balancing of target properties and leads to a final BOP for Re. The final BOP is shown to give robust predictions for elastic constants, phonons, point defects, stacking faults, and the energetic ordering of various crystal structures. An analysis of the final BOP with the RMS error across the entire phase space of one-atom unit cells highlights the compromise between local accuracy and global transferability.

Details of the parametrization protocol are specific to BOP and Re but the overall concepts are generally applicable to the parametrization of interatomic potentials. In particular, the parametrization protocol has already been used to develop analytic BOPs in order to study phase transitions in Ti [36], to demonstrate the stabilizing effect of magnetism on ordered Fe-Co alloys [32], and to rationalize the experimentally observed segregation of Re to partial dislocations in Ni [37].

ACKNOWLEDGMENTS

We acknowledge financial support by the German Research Foundation (DFG) through research Grant No. HA 6047/4-1 (Project No. 289654611) and project C1 of the collaborative research center SFB/TR 103 (Project No. 190389738).

[1] P. Brommer and F. Gähler, Potfit: Effective potentials from ab initio data, Modell. Simul. Mater. Sci. Eng. **15**, 295 (2007).

[2] A. Jaramillo-Botero III, S. Naserifar, and W. A. Goddard, General multiobjective force field optimization framework, with application to reactive force fields for silicon carbide, J. Chem. Theor. Comput. **10**, 1426 (2014).

[3] A. I. Duff, M. Finnis, P. Maugis, B. J. Thijsse, and M. H. Sluiter, MEAMfit: A reference-free modified embedded atom

method (RF-MEAM) energy and force-fitting code, Comput. Phys. Commun. **196**, 439 (2015).
[4] C. D. Barrett and R. L. Carino, The MEAM parameter calibration tool: an explicit methodology for hierarchical bridging between ab initio and atomistic scales, Integr. Mater. Manuf. Innov. **5**, 177 (2016).
[5] C.-P. Chou, Y. Nishimura, C.-C. Fan, G. Mazur, S. Irle, and H. A. Witek, Automatized parameterization of DFTB using particle swarm optimization, J. Chem. Theor. Comput. **12**, 53 (2016).
[6] A. Stukowski, E. Fransson, M. Mock, and P. Erhart, Atomicrex—a general purpose tool for the construction of atomic interaction models, Modell. Simul. Mater. Sci. Eng. **25**, 055003 (2017).
[7] A. Ladines, T. Hammerschmidt, and R. Drautz, BOPcat software package for the construction and testing of tight-binding models and bond-order potentials, Comput. Mater. Sci. **173**, 109455 (2020).
[8] M. W. Finnis and J. E. Sinclair, A simple empirical n-body potential for transition metals, Philos. Mag. A **50**, 45 (1984).
[9] M. S. Daw and M. I. Baskes, Embedded-atom method: Derivation and application to impurities, surfaces, and other defects in metals, Phys. Rev. B **29**, 6443 (1984).
[10] F. H. Stillinger and T. A. Weber, Computer simulation of local order in condensed phases of silicon, Phys. Rev. B **31**, 5262 (1985).
[11] J. Tersoff, New empirical model for the structural properties of silicon, Phys. Rev. Lett. **56**, 632 (1986).
[12] D. G. Pettifor, Pressure-cell boundary relation and application to transition-metal equation of state, Commun. Phys. **1**, 141 (1976).
[13] A. P. Sutton, M. W. Finnis, D. G. Pettifor, and Y. Ohta, The tight-binding bond model, J. Phys. C **21**, 35 (1988).
[14] D. Porezag, T. Frauenheim, T. Köhler, G. Seifert, and R. Kaschner, Construction of tight-binding-like potentials on the basis of density-functional theory: Application to carbon, Phys. Rev. B **51**, 12947 (1995).
[15] M. Elstner, D. Porezag, G. Jungnickel, J. Elsner, M. Haugk, T. Frauenheim, S. Suhai, and G. Seifert, Self-consistent-charge density-functional tight-binding method for simulations of complex materials properties, Phys. Rev. B **58**, 7260 (1998).
[16] D. G. Pettifor, New many-body potential for the bond-order, Phys. Rev. Lett. **63**, 2480 (1989).
[17] A. P. Horsfield, A. M. Bratkovsky, M. Fearn, D. G. Pettifor, and M. Aoki, Bond-order potentials: Theory and implementation, Phys. Rev. B **53**, 12694 (1996).
[18] T. Hammerschmidt, R. Drautz, and D. G. Pettifor, Atomistic modelling of materials with bond-order potentials, Int. J. Mater. Res. **100**, 1479 (2009).
[19] R. Drautz, T. Hammerschmidt, M. Cak, and D. G. Pettifor, Bond-order potentials: Derivation and parameterization for refractory elements, Modell. Simul. Mater. Sci. Eng. **23**, 074004 (2015).
[20] J. J. Möller, M. Mrovec, I. Bleskov, J. Neugebauer, T. Hammerschmidt, R. Drautz, C. Elsässer, T. Hickel, and E. Bitzek, On {110} planar faults in strained bcc metals-origins and implications of a commonly observed artefact of classical potentials, Phys. Rev. Mater. **2**, 093606 (2018).
[21] Y. Lysogorskiy, T. Hammerschmidt, J. Janssen, J. Neugebauer, and R. Drautz, Transferability of interatomic potentials for molybdenum and silicon, Modell. Simul. Mater. Sci. Eng. **27**, 025007 (2019).
[22] S. Starikov, D. Smirnova, T. Pradhan, Y. Lysogorskiy, H. Chapman, M. Mrovec, and R. Drautz, Angular-dependent interatomic potential for large-scale atomistic simulation of iron: Development and comprehensive comparison with existing interatomic models, Phys. Rev. Mater. **5**, 063607 (2021).
[23] R. Drautz and D. G. Pettifor, Valence-dependent analytic bond-order potential for transition metals, Phys. Rev. B **74**, 174117 (2006).
[24] M. Mrovec, D. Nguyen-Manh, D. G. Pettifor, and V. Vitek, Bond-order potential for molybdenum: Application to dislocation behaviour, Phys. Rev. B **69**, 094115 (2004).
[25] M. Mrovec, R. Gröger, A. G. Bailey, D. Nguyen-Manh, C. Elsässer, and V. Vitek, Bond-order potential for simulations of extended defects in tungsten, Phys. Rev. B **75**, 104119 (2007).
[26] G. K. H. Madsen, E. J. McEniry, and R. Drautz, Optimized orthogonal tight-binding basis: Application to iron, Phys. Rev. B **83**, 184119 (2011).
[27] M. Mrovec, D. Nguyen-Manh, C. Elsässer, and P. Gumbsch, Magnetic bond-order potential for iron, Phys. Rev. Lett. **106**, 246402 (2011).
[28] E. J. McEniry, G. K. H. Madsen, J. F. Drain, and R. Drautz, Tight-binding simulation of transition-metal alloys, J. Phys.: Condens. Matter **23**, 276004 (2011).
[29] Y.-S. Lin, M. Mrovec, and V. Vitek, A new method for development of bond-order potentials for transition bcc metals, Modell. Simul. Mater. Sci. Eng. **22**, 034002 (2014).
[30] M Čák, T. Hammerschmidt, J. Rogal, V. Vitek, and R. Drautz, Analytic bond-order potentials for the bcc refractory metals Nb, Ta, Mo and W, J. Phys.: Condens. Matter **26**, 195501 (2014).
[31] M. Ford, R. Drautz, T. Hammerschmidt, and D. G. Pettifor, Convergence of an analytic bond-order potential for collinear magnetism in Fe, Modelling Simul. Mater. Sci. Eng. **22**, 034005 (2014).
[32] A. Egorov, A. P. A. Subramanyam, Z. Yuan, R. Drautz, and T. Hammerschmidt, Magnetic bond-order potential for iron-cobalt alloys, Phys. Rev. Mater. **7**, 044403 (2023).
[33] A. Girshick, A. M. Bratkovsky, D. G. Pettifor, and V. Vitek, Atomistic simulation of titanium. I. A bond-order potential, Philos. Mag. A **77**, 981 (1998).
[34] S. Znam, D. Nguyen-Manh, D. G. Pettifor, and V. Vitek, Atomistic modelling of TiAl: I. Bond-order potentials with environmental dependence, Philos. Mag. **83**, 415 (2003).
[35] M. J. Cawkwell, D. Nguyen-Manh, D. G. Pettifor, and V. Vitek, Construction, assessment, and application of a bond-order potential for iridium, Phys. Rev. B **73**, 064104 (2006).
[36] A. Ferrari, M. Schröder, Y. Lysogorskiy, J. Rogal, M. Mrovec, and R. Drautz, Phase transitions in titanium with an analytic bond-order potential, Modell. Simul. Mater. Sci. Eng. **27**, 085008 (2019).
[37] S. Katnagallu, L. Stephenson, I. Mouton, C. Freysoldt, A. Subramanyam, J. Jenke, A. Ladines, S. Neumeier, T. Hammerschmidt, R. Drautz, J. Neugebauer, F. Vurpillot, D. Raabe, and B. Gault, Imaging individual solute atoms at crystalline imperfections in metals, New J. Phys. **21**, 123020 (2019).
[38] J. Jenke, A. N. Ladines, T. Hammerschmidt, D. G. Pettifor, and R. Drautz, Tight-binding bond parameters for dimers across the periodic table from density-functional theory, Phys. Rev. Mater. **5**, 023801 (2021).

[39] J. Jenke, A. P. A. Subramanyam, M. Densow, T. Hammerschmidt, D. G. Pettifor, and R. Drautz, Electronic structure based descriptor for characterizing local atomic environments, Phys. Rev. B **98**, 144102 (2018).

[40] C. Rae and R. Reed, The precipitation of topologically close-packed phases in rhenium-containing superalloys, Acta Mater. **49**, 4113 (2001).

[41] A. V. Naumov, Rhythms of rhenium, Russ. J. Non-Ferrous Met. **48**, 418 (2007).

[42] M. Gilbert and J.-C. Sublet, Neutron-induced transmutation effects in w and w-alloys in a fusion environment, Nucl. Fusion **51**, 043005 (2011).

[43] O. Levy, M. Jahnátek, R. V. Chepulskii, G. L. W. Hart, and S. Curtarolo, Ordered structures in rhenium binary alloys from first-principles calculations, J. Am. Chem. Soc. **133**, 158 (2011).

[44] A. Hasegawa, M. Fukuda, S. Nogami, and K. Yabuuchi, Neutron irradiation effects on tungsten materials, Fusion Eng. Des. **89**, 1568 (2014).

[45] M. Fukuda, K. Yabuuchi, S. Nogami, A. Hasegawa, and T. Tanaka, Microstructural development of tungsten and tungsten–rhenium alloys due to neutron irradiation in hfir, J. Nucl. Mater. **455**, 460 (2014).

[46] M. Lloyd, A. London, J. Haley, M. Gilbert, C. Becquart, C. Domain, E. Martinez, M. Moody, P. Bagot, D. Nguyen-Manh, and D. Armstrong, Interaction of transmutation products with precipitates, dislocations and grain boundaries in neutron irradiated w, Materialia **22**, 101370 (2022).

[47] G. Bonny, A. Bakaev, D. Terentyev, and Y. A. Mastrikov, Interatomic potential to study plastic deformation in tungsten-rhenium alloys, J. Appl. Phys. **121**, 165107 (2017).

[48] W. Setyawan, N. Gao, and R. J. Kurtz, A tungsten-rhenium interatomic potential for point defect studies, J. Appl. Phys. **123**, 205102 (2018).

[49] T. Hammerschmidt, B. Seiser, M. E. Ford, A. N. Ladines, N. Wang, J. Jenke, Y. Lysogorskiy, C. Teijeiro, M. Mrovec, M. Čák, E. R. Margine, D. G. Pettifor, and R. Drautz, BOPfox program for tight-binding and analytic bond-order potential calculations, Comput. Phys. Commun. **235**, 221 (2019).

[50] F. Cyrot-Lackmann, On the electronic structure of liquid transition metals, Adv. Phys. **16**, 393 (1967).

[51] D. Nguyen-Manh, D. Pettifor, S. Znam, and V. Vitek, Negative cauchy pressure within the tight-binding approximation, in *Tight-binding Approach to Computational Materials Science*, edited by P. Turchi, A. Gonis, and L. Colombo (Materials Research Society, 1998), pp. 353–358.

[52] M. Aoki and T. Kurokawa, A simple environment-dependent overlap potential and Cauchy violation in solid argon, J. Phys.: Condens. Matter **19**, 236228 (2007).

[53] K. Levenberg, A method for the solution of certain non-linear problems in least squares, Q. Appl. Math. **2**, 164 (1944).

[54] D. W. Marquardt, An algorithm for least-squares estimation of nonlinear parameters, J. Soc. Indust. Appl. Math. **11**, 431 (1963).

[55] J. J. Moré, The Levenberg-Marquardt algorithm: Implementation and theory, in *Numerical Analysis*, edited by G. A. Watson, Lecture Notes in Mathematics Vol. 630 (Springer, Berlin, Heidelberg, 1978), pp. 105–116.

[56] G. Kresse and J. Furthmüller, Efficiency of ab-initio total energy calculations for metals and semiconductors using a plane-wave basis set, Comput. Mater. Sci. **6**, 15 (1996).

[57] G. Kresse and J. Furthmüller, Efficient iterative schemes for *ab initio* total-energy calculations using a plane-wave basis set, Phys. Rev. B **54**, 11169 (1996).

[58] G. Kresse and D. Joubert, From ultrasoft pseudopotentials to the projector augmented-wave method, Phys. Rev. B **59**, 1758 (1999).

[59] P. E. Blöchl, Projector augmented-wave method, Phys. Rev. B **50**, 17953 (1994).

[60] J. P. Perdew, K. Burke, and M. Ernzerhof, Generalized gradient approximation made simple, Phys. Rev. Lett. **77**, 3865 (1996).

[61] H. J. Monkhorst and J. D. Pack, Special points for Brillouin-zone integrations, Phys. Rev. B **13**, 5188 (1976).

[62] T. Hammerschmidt, A. F. Bialon, D. G. Pettifor, and R. Drautz, Topologically close-packed phases in binary transition-metal compounds: Matching high-throughput ab initio calculations to an empirical structure map, New J. Phys. **15**, 115016 (2013).

[63] J. Janssen, S. Surendralal, Y. Lysogorskiy, M. Todorova, T. Hickel, R. Drautz, and J. Neugebauer, pyiron: An integrated development environment for computational materials science, Comput. Mater. Sci. **163**, 24 (2019).

[64] G. Henkelman, B. P. Uberuaga, and H. Jónsson, A climbing image nudged elastic band method for finding saddle points and minimum energy paths, J. Chem. Phys. **113**, 9901 (2000).

[65] G. Henkelman and H. Jónsson, Improved tangent estimate in the nudged elastic band method for finding minimum energy paths and saddle points, J. Chem. Phys. **113**, 9978 (2000).

[66] D. Hull and D. Bacon, *Introduction to Dislocations* (Butterworth-Heinemann, Oxford, 2011).

[67] Q.-M. Hu and R. Yang, Basal-plane stacking fault energy of hexagonal close-packed metals based on the ising model, Acta Mater. **61**, 1136 (2013).

[68] B. Yin, Z. Wu, and W. Curtin, Comprehensive first-principles study of stable stacking faults in hcp metals, Acta Mater. **123**, 223 (2017).

[69] D. G. Pettifor, The structures of binary compounds: I. Phenomenological structure maps, J. Phys. C **19**, 285 (1986).

[70] D. G. Pettifor, *Bonding and Structure of Molecules and Solids* (Oxford Science, 1995).

[71] B. Seiser, T. Hammerschmidt, A. N. Kolmogorov, R. Drautz, and D. G. Pettifor, Theory of structural trends within 4*d* and 5*d* transition metal topologically close-packed phases, Phys. Rev. B **83**, 224116 (2011).

[72] P. E. A. Turchi, Interplay between local environment effect and electronic structure properties in close packed structures, MRS Symposium Proceedings No. 206 (MRS, 1990), p. 265.

[73] T. Hammerschmidt, A. N. Ladines, J. Koßmann, and R. Drautz, Crystal-structure analysis with moments of the density-of-states: Application to intermetallic topologically close-packed phases, Crystals **6**, 18 (2016).

[74] C. Sutton, L. Giringhelli, T. Yamamoto, Y. Lysogorkiy, L. Blumenthal, T. Hammerschmidt, J. Golebiowski, X. Liu, A. Ziletti, and M. Scheffler, Crowd-source materials-science challenges with the NOMAD2018 Kaggle competition, npj Comput. Mater. **5**, 111 (2019).